Journal of Nano Research
ISSN: 1661-9897, Vol. 63, pp 10-30

Submitted: 2020-01-14
Accepted: 2020-04-29
Online: 2020-06-10

Effect of Solution Concentration on ZnO/$ZnAl_2O_4$ Nanocomposite Thin Films Formation Deposited by Ultrasonic Spray Pyrolysis on Glass and Si(111) Substrates

Sabrina IAICHE[1,a*], Chahra BOUKAOUS[2,b], David ALAMARGUY[3,c], Abdelkader DJELLOUL[1,d] and Djamel HAMANA[4,e]

[1]Laboratory of Structures, Proprieties and Inter Atomic Interactions (LASPI²A), Faculty of Science and Technology, University of Abbes Laghrour, Khenchela 40000, Algeria.

[2]Laboratoire Microsystème et Instrumentation, Département d'électronique, Université de Constantine 1, route d'Ain El Bey, 25000 Constantine, Algeria.

[3]GeePs | Group of electrical engineering - Paris, CNRS, CentraleSupélec, Univ. Paris-Sud, Université Paris-Saclay, Sorbonne Université, 3 & 11 rue Joliot-Curie, Plateau de Moulon 91192 Gif-sur-Yvette CEDEX, France.

[4]Research Unit in materials science and applications, Constantine 1 University and material engineering department, National Polytechnic Institute of Constantine, BP 75, A, Nouvelle ville RP, Ali Mendjeli, 25000 Constantine - Algeria.

[a]sabrina_iaiche@yahoo.fr, [b]ch_boukaous@yahoo.fr, [c]david.alamarguy@supelec.fr, [d]djelloulabdelkader@yahoo.fr, [e]d_hamana@yahoo.fr

Keywords: ZnO_$ZnAl_2O_4$ thin film, molarities, Si(111), Si(100), glass substrate, XRD, Raman spectroscopy, Zn_2SiO_4, USP

Abstract. A complex ZnO/$ZnAl_2O_4$ heterostructures thin films on glass and Si(111) substrates have been successively obtained by a soft ultrasonic spray pyrolysis (USP) method deposition using the Zn/Al molar ratios concentrations of 0.07/0.13 and 0.1/0.1, respectively. According to (XRD) an ordered zinc oxide (ZnO) and zinc aluminate ($ZnAl_2O_4$) structures deposited onto glass from the air annealing at 500 °C during 2 hours was observed and confirmed by the (EDX), (FTIR) and Raman spectroscopy techniques. The estimated crystallites size and stress values of ZnO and $ZnAl_2O_4$ in the ZnO/$ZnAl_2O_4$/glass film were 19 nm/0.469 GPa and 11 nm/-0.292 GPa, respectively. The lower Zn/Al molar ratio around 0.035/0.06 produced only ZnO as a single phase, suggesting the Al insufficient quantity. The Si(100) substrate with 0.07 Zn molarity conducted to the Zn_2SiO_4/ZnO/$ZnAl_2O_4$ composite. The Raman integrated intensity bands of ZnO and $ZnAl_2O_4$ increases with increasing Zn to Al molar ratio (0.1/0.1 comparatively to 0.07/0.13). The ZnO&$ZnAl_2O_4$ crystallinity enhances as Zn molarity increases. The ZnO films in the composites grow with (002) texture. The *TC(hkl)* value indicated that $ZnAl_2O_4$ in the ZnO/$ZnAl_2O_4$/glass layer is polycrystalline preferentially oriented along the (311) plane. Spinel $ZnAl_2O_4$ oxide onto Si(111) substrate grown according to the (220) orientation. Crystallites are larger in ZnO/$ZnAl_2O_4$/Si than in ZnO/$ZnAl_2O_4$/glass. The ZnO/$ZnAl_2O_4$ film onto glass substrate is transparent in the visible and near infrared regions and sensitive to UV absorption, as characterized by UV-Vis spectroscopy. The ZnO and $ZnAl_2O_4$ E_g values in the ZnO/$ZnAl_2O_4$/glass composite were 3.25 and 3.88 eV, respectively.

1. Introduction

The degradation of pollutants by photocatalytic reactions in general, occurs and enhances under UV radiations, with semiconductor photocatalysts excited and e^- and h^+ pairs generated [1]. The photocatalytic activity of the catalysts is highly dependent on the pollutant adsorption behavior and the separation efficiency of the electron-hole pairs [2]. The coupling between ZnO, which is an excellent photocatalyst for the degradation of organic and inorganic pollutants as well as hazardous waste in water and air, due to its photo-sensitivity, non-toxicity and its direct 3.37 eV at room temperature and indirect 2.45 eV optical gap values, with a second non-sensitive wide band gap semiconductor proved that was an effective method to improve their photocatalytic activities [1, 3].

In particular the well-formed band structure between ZnO and $ZnAl_2O_4$ (E_g = 3.8 eV) oxides facilitates the migration of photogenerated carriers, thereby ensures the separation efficiency of photogenerated pairs across the heterojunction interface of the composite by injecting electrons into the lower lying conduction band of the large bandgap semiconductor [1, 4]. Kumar et al. reported that the nanocomposite ZnO/$ZnAl_2O_4$ is energetically favorable in suppressing the recombination of photogenerated electrons and holes due the presence of the spinel phase with high surface area and thermal stability [5]. As it is known, the photocatalytic activities of photocatalysts are enhanced with reducing their size, due to its higher surface to volume ratio as compared to bulk materials. The ZnO/$ZnAl_2O_4$ system is used as catalyst [3, 6] and adsorbent support for environmental remediation and waste degradation of biological materials [7], in the de-colorization of textile pollutants; such as methyl orange (MO) [1, 3, 8] and methylene blue (MB) under UV irradiation where the oxides mixture exhibits a better and much higher catalytic performance than the ZnO alone [1, 3, 9]. From biological application (biochemistry, food industry, clinical diagnosis and environmental engineering) point of view, both ZnO and $ZnAl_2O_4$ are biocompatible for sensitive bio-analysis and efficient bio-catalysis as the alkaline phosphatase (ALP) enzyme immobilization [10]. It is also estimated that the composite ZnO/$ZnAl_2O_4$ is promising for improving gas sensing properties considering synergistic effects between one another and the catalytic property of $ZnAl_2O_4$ [11]. According to M. Hoppe et al., M–Y. Guan et al. and R. Huo et al. the ZnO/$ZnAl_2O_4$ mist oxides has a high potential as sensors of pollutants, toxic and combustible gas like hydrogen (H_2) [12] ethanol (CH_3CH_2OH) [11, 12] or ammoniac (NH_3) [13] with superior response to many reported performances of other individual metal oxide nanostructures [12]. The integration of functional oxides on Si substrates could open a pathway to integrate diverse devices on Si-based technology, in particular the development of conductometric gas sensors based on nanocomposites. Meanwhile ZnO/$ZnAl_2O_4$ film deposited on amorphous or conducting materials by spray pyrolysis technique may have large surface area and potentials application in catalysts and gas sensing.

Zinc aluminate (gahnite, $ZnAl_2O_4$) is a spinel-type complex oxide. This compound is nontoxic, inexpensive and very stable material. $ZnAl_2O_4$ is widely used as electronic, ceramic and catalytic material [14]. $ZnAl_2O_4$ is suitable for UV optoelectronic applications, thermal and optical control coatings, as transparent conductor and for new generation of bioceramics in dental implant and bone substitute applications [15]. It is used as an excellent fluorescent devices [16], as a gas sensor (O_3 and CO) [17, 18], in many catalytic reactions and as an efficient photocatalyst [19]. $ZnAl_2O_4$ is of interest due to its combination of desirable properties such as high mechanical resistance, high thermal and chemical stability, high fluorescence efficiency, high photocatalytic activity and low surface acidity [20].

Zinc silicate (willemite, α-Zn_2SiO_4) is a very important phosphor material and widely used in optic, optoelectronic and lighting devices [21, 22]. It is used as an electrical insulators, catalysts support, glazes, pigments, radiation detectors in medical imaging systems and phosphors host in electronic systems [23]. Zn_2SiO_4 is a wide band gap (E_g = 5.5 eV) oxide possess fascinating luminescent and physicochemical properties, such as good chemical stability, mechanical strength, thermal conductivity and low coefficient of thermal expansion, color purity, and better wear resistance [22]. Zinc silicate exists in three structural polymorphs. i.e. α-, β-, γ-Zn_2SiO_4. The β-, and γ- forms are metastable phases which transform to α - (willemite) phase at high temperature [23]. Usually, willemite is obtained by conventional solid-state method in which well mixed ZnO and SiO_2 raw materials are fired at very high temperatures for several hours [21]. The production of Zn_2SiO_4 using waste material such as glass waste or Si wafer as a silicon source is also possible [21, 24]. The annealing of the Si/ZnO or SiO_2/ZnO systems can lead to the formation of willemite Zn_2SiO_4 oxide [24], but need to be controllable. However, growth of Zn_2SiO_4 with high crystalline phase is still challengeable [22].

In this work, a study of the nanocomposite ZnO/$ZnAl_2O_4$ thin films realized by engineering the initial salts quantities in correlation with silicon and glass substrates effect is developed. The paper is so a contribution to the thorough and simple strategy deposition of the functional complex oxides films, for a larger application, as well as the investigation of the structural and optical properties.

2. Experimental

The chemical pyrolysis deposition technique was employed by spraying of the mixture solutions based on zinc chloride ($ZnCl_2$) and aluminum acetate ($C_2H_5AlO_4$) salts (99,9% purity Fulka) with Zn/Al molar concentrations of 1:2 ($R_1 \sim 0.07/0.13$) and 1:1 ($R_2 \sim 0.13/0.13$) respectively. USP is beneficial towards its low cost, a better stoichiometry control and homogeneity, covering large area films, soft starting materials and having an easy coating process of large substrates. $ZnCl_2$ was dissolved in deionized water and $C_2H_5AlO_4$ in (30 ml CH_3OH + 20 ml C_2H_5OH + 150 ml H_2O), ethanol and methanol are volatile and thus facilitate transformation of precursor into vapor form. A small amount of acetic acid (CH_3COOH) was added to aqueous solutions to prevent the formation of hydroxides. The two solutions was mixed and maintained under magnetic stirrer agitation at low temperature (below 100°C) for 3 h. The agitation promoted the chemical reaction between precursors, facilitating the dissolution of the salts and maintaining the high homogeneity of the mixed solutions. The spray solution is carried through an ultrasonic pyrolysis system that converts into fine droplets. The ultrasonic vibrator frequency was 40 kHz and the power used was 130 W (Ultrasonic atomizer VCX 134 AT). These solutions were sprayed onto glass and silicon substrates placed below a substrate holder heated to a fixed temperature of 450°C. The solution flow rate was held constant at 10 ml/h. The nozzle-substrate distance was 7 cm. The time deposition was 03h20min. After deposition, the samples were annealed in air for 2 hours at 500°C. The phase and crystalline orientation of the obtained layers was investigated using X-ray diffraction (XRD) on a Schimadzu XRD 6000 diffractometer with Cu-K_α radiation (λ = 0.15406 nm). The chemical bending states and kinetic studies of the films were probed by using Raman spectroscopy and Fourier transform infrared (FTIR) spectrometry at room temperature. FTIR spectra of the samples were collected in absorbance mode by using a Perkin-Elmer Frontier FTIR spectrometer. The pellet for FTIR measurement was prepared by grinding the film scraped from the glass substrate and 1% weight of KBr to weight of sample. Measurement resolution was 4 cm^{-1}. The Raman spectrometer used in this study on the silicon support coated samples was a Jobin Yvon Technology Olympus BX 41/Horiba scientific system LabRAM HR Evolution. The 473.1 nm wavelength line from a solid state Nd:YAG blue laser was used as the excitation source for analyzed Si support films. A filter wheel reduced the output laser power to 12 mW on the samples. The laser spot size was ~ 20 and the time of acquisition was 20 s. For the layer deposited on glass, the excitation source was the 532 nm wavelength.

3. Results and Discussion

Figures 1(a) and (b) present the XRD patterns of the 500°C during 2 hours air-annealed film deposited on glass substrate. The crystallization of the ZnO hexagonal phase with a wurtzite structure and the $ZnAl_2O_4$ phase with a cubic structure occured according to (Joint Committee on Powder Diffraction Standards (JCPDS) PDF numbers 00-036-1451 and 01-073-1961 respectively) is noted. No impurities and other pics were observed reflecting the high purity of the ZnO/$ZnAl_2O_4$ coating. ZnO and $ZnAl_2O_4$ structures are polycrystalline by the presence of a multitude of (hkl) planes. The ZnO and $ZnAl_2O_4$ diffraction peaks on figure 1(a) are narrow and exhibit an important intensity, which suggests that the oxides have a good crystalline quality.

Deconvolution of the obtained XRD spectrum in the 2θ range between 29 and 39 degrees of the glass coated film into a series of separated peaks was done in order to accurately determine the position of each peak, figure 1(b), assigns the presence of the diffraction peak corresponding to the ZnO (101) plane. Indeed, on the diffractogram, the asymmetric major peak consists of two peaks positioned at 36.229° and 36.856° corresponding to the (101)/ZnO and (311)/$ZnAl_2O_4$ planes, respectively. The diffraction peak (220)/$ZnAl_2O_4$ positioned at 31.311° does not support any shoulder corresponding to the (100)/ZnO plane by the de-convolution, suggesting that the growth of the ZnO phase is closely related to that of spinel. The annealing temperature of 500°C can be considered as low for the simultaneous good crystalline order of the two phases, it is noted that with an annealing at 450 °C - 2h the film is amorphous (diffractogram not reported).

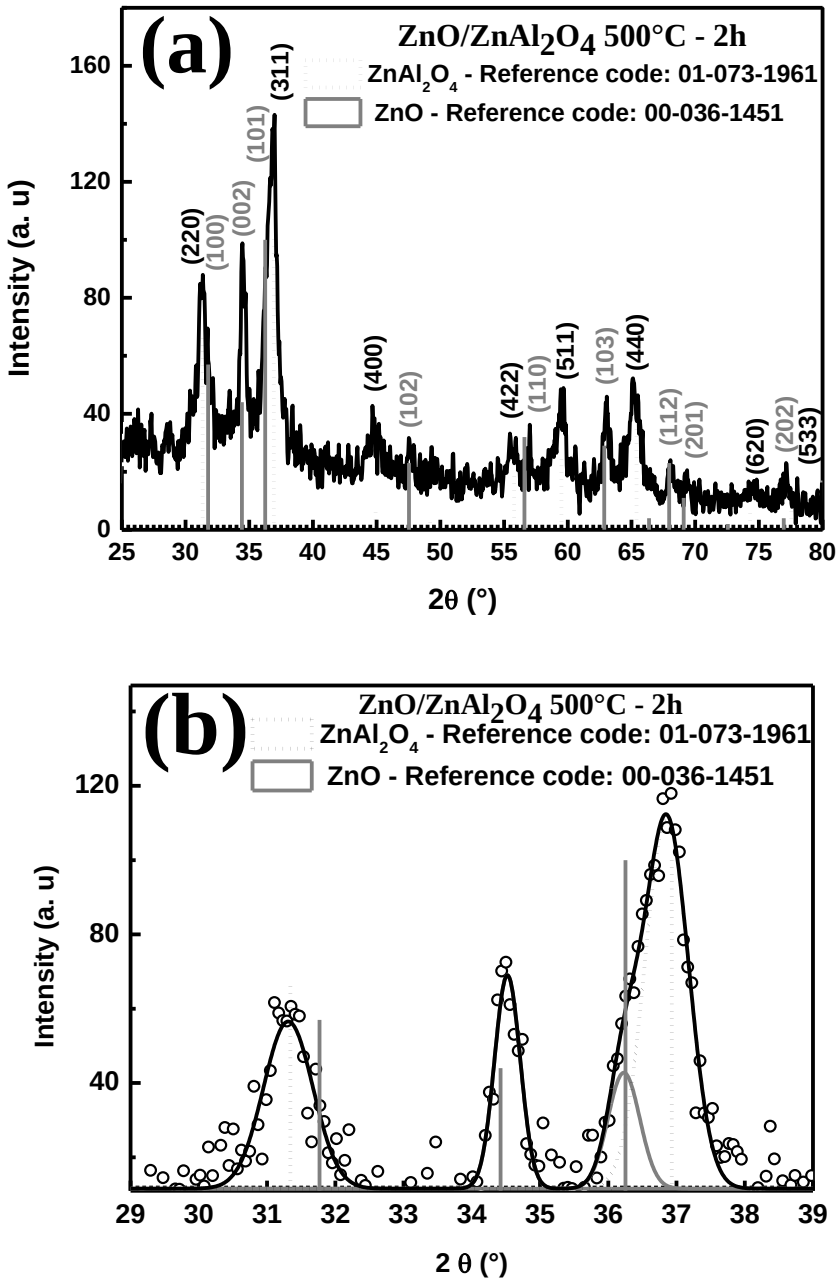

Fig. 1. XRD patterns of ZnO_$ZnAl_2O_4$ film deposited on glass substrate with Zn/Al molar ratio R_1 ~ 0.07/0.13 and air-annealed at 500°C/2h (a) scanning 2θ = 25-80° and (b) 29-39° data's deconvolution.

Table 1. Results of the peak de-convolution by the functions $I(x) \propto \frac{A}{w\sqrt{\pi/2}} \exp\left(-2\left(\frac{x-x_C}{w}\right)^2\right)$(2), $FWHM = w\sqrt{2\ln(2)}$ (3) and several structural parameters of the ZnO/$ZnAl_2O_4$ film deposited on glass substrate and annealed at 500°C.

Annealing Temperature	Deconvolution result	ZnO			$ZnAl_2O_4$	
		(100)	(002)	(101)	(220)	(311)
500°C	y_0	/	11.563	11.563	11.563	11.563
	x_c	/	34.522	36.228	31.310	36.855
	W	/	0.376	0.467	0.724	0.642
	A	/	27.110	18.274	40.826	80.436
	Sigma	/	0.188	0.233	0.362	0.321
	FWHM	/	0.443	0.549	0,852	0.756
	Height	/	57.457	31.220	44.993	99.905
	I (%)		100.0	54.3	45,0	100.0
	TC	/	1.61	0.38	0.81	1.19
	D, nm		19			11
	a, nm		0.325			0.808
	c, nm		0.519			
	ε%		-0.201			0.280
	σ, GPa		0.469			-0.292
DRX standard	2Θ (°)	31.770	34.422	36.253	31.342	36.931
	I (%)	57.0	44.0	100.0	66.1	100.0

The annealing of the ZnO/$ZnAl_2O_4$ layer may influence the growth orientation of the structures. The study of this effect is done by analyzing the intensities using the *TC*(*hkl*) texture coefficient. Depending on *TC* values, we can determine the preferred orientation of the layer. When 0 <*TC(hkl)* <1: absence of the layer preferred orientation in the (hkl) direction. If *TC* = 1: the layer is polycrystalline with no preferential orientation. When *TC(hkl)*> 1: the layer is polycrystalline with a preferred orientation according to the (hkl) plane.

The *TC(hkl)* values of our film (see Table 1) are calculated using the following formula [25]:

$$TC(hkl) = \frac{I(hkl)/I_0(hkl)}{(1/n)\sum_n I(hkl)/I_0(hkl)} \quad (1)$$

Where *I(hkl)* and *I_0(hkl)* are respectively the relative intensity of the (hkl) peak and the standard intensity of the (hkl) peak given in the JCPDS cards, n is the number of diffraction peaks.

The *TC(hkl)* values show that the ZnO crystallites in ZnO/$ZnAl_2O_4$ have a preferential orientation following the (002) plane along the '*c*' axis. The surface energy is the smallest for the crystal in the case of an (002) orientation [26]. When the temperature increases, the atoms have enough diffusion activation energy to occupy the correct site in the crystal lattice, which results in an increase in the crystallinity and the grains size [27]. Then the growth orientation develops into one crystallographic direction of the low surface energy, leading to the increases of ZnO grain sizes [26], which is in agreement with our result. The ZnO *c*-axis orientation growth is due to the improvement of stoichiometry [28]. Therefore, eh et al. assumed that in the first stage of heat treatment of ZnO, crystalline centers nucleated, coalesce with each other and grow into large grains [29]. The *TC(hkl)* value, also indicate that $ZnAl_2O_4$ in the ZnO/$ZnAl_2O_4$ layer is polycrystalline preferentially oriented along the (311) plane. In the ZnO hexagonal structure, the lattice constants '*a*' and '*c*' were calculated by using equations (4) and (5) [30] and in the $ZnAl_2O_4$ cubic one, the lattice constant '*a*' was determined by using formula (6) [31]:

$$d_{hkl} = \frac{1}{\sqrt{\frac{4(h^2+k^2+hk)}{3a^2} + \frac{l^2}{c^2}}} \quad (4) \quad d_{hkl} = \frac{\lambda}{2\sin\theta_{hkl}} \quad (5)$$

$$d_{hkl} = \frac{a}{\sqrt{h^2+k^2+l^2}} \quad (6)$$

where d_{hkl} is the spacing between lattice planes of Miller indices (h, k and l).

Information on the crystallites size (D) for the films was obtained from the full width at half maximum of the diffraction peaks using the Scherrer formula (7) [31]:

$$D = \frac{0.94\lambda}{\beta_{(hkl)}\cos\theta_{(hkl)}} \quad (7)$$

where λ, (hkl), and $\beta(hkl)$ are the X-ray wavelength (0.15418 nm), Bragg diffraction angle, and line width at half maximum, respectively. The crystallites size and the microdeformation in the ZnO and $ZnAl_2O_4$ films were calculated from the integral width and the position of the (002) and (311) peaks, respectively. The average crystallites size of the 500°C annealed film are listed in Table 1. The crystallites size of ZnO and $ZnAl_2O_4$ were evaluated to be 19 and 11 nm, respectively. According to previous papers [26, 28, 30] related to the growth of the ZnO nanoparticles of single-phase films, the ZnO nanoparticles size is in general increased by raising the annealing temperature which could lead to migration of grain boundaries resulting in coalescence of crystallites to one another as being annealed. The mergin process of the ZnO nanoparticles is favoured by the zinc or oxygen defects at the grain boundaries [30]. Lattice parameters values of the ZnO structure obtained at the annealing temperature ~ 500°C are very close to the a and c values for ZnO polycrystalline powder (a = 3.2498 Å, c = 5.2066 Å) [30, 32], indicating that the film is displaying a low degree distortion.

The evaluation of the average uniform stress in the ZnO film is based on the biaxial stress model [33]. The microdeformation ε, along the c-axis perpendicular to the substrate surface has been estimated from the X-ray diffraction data using the following expression (8) :

$$\varepsilon = (c_{film} - c_{bulk}) \times 100\% = \frac{\Delta c}{c} \times 100\% \quad (8)$$

where c_{bulk} and c_{film} are the lattice parameters of the ZnO standard powder (bulk) ; also called the unstrained lattice parameter (c_{bulk} = 0.52069 *nm*) and the prepared film. For hexagonal crystals, the stress σ_{film} in the plane of the film can be calculated using the equation (9):

$$\sigma_{film}^{XRD} = \frac{2C_{13}^2 - C_{33}(C_{11}+C_{12})}{2C_{13}} \times \frac{c_{film} - c_{bulk}}{c_{bulk}} \quad (9)$$

For the elasctic stiffness constants C_{ij}, the data of bulk single crystal ZnO wich have been used C_{11} = 208.8 GPa, C_{33} = 213.8 GPa, C_{12} = 119.7 GPa, C_{13} = 104.2 GPa [33]. This gives the following numerical stress relationship (7) from the XRD: $\sigma_{film} = -233\varepsilon$ $[GPa]$ [30].

The value of residual stresses of the $ZnAl_2O_4$ films has been obtained from the following equation (10) [34]:

$$\frac{1+\nu}{2E}\sigma_{film}^{XRD} = \frac{a_{45°} - a_{0°}}{a_0} \quad (10)$$

E is the Young's modulus, ν is the Poisson coefficient, a_0 is the lattice constant of the bulk material, $a_{45°}$ is the lattice constant measured using an asymmetric tilted 45° analysis and $a_{0°}$ is the lattice constant measured using a symmetric $\theta/2\theta$ scan. The values of E and ν reported for $ZnAl_2O_4$

[35] which were used (E = 193 GPa and ν = 0.3241). The estimated values of stress ''σ'' in the ZnO and $ZnAl_2O_4$ structures in the $ZnO/ZnAl_2O_4$ composite are listed in Table 1.

The residual stress of ZnO layer in the $ZnO/ZnAl_2O_4$ nanocomposite is tensile and for $ZnAl_2O_4$ is compressive. In addition, the position of the (002) diffraction peak is shifted towards the upper angle where the cell constant *c* is reduced [33]. The decrease in lattice parameters was attributed according to Usseinov et al. to the variation in nature and concentration of the native imperfections which causes their compression [36]. ZnO nanostructures can typically have a number of defects such as oxygen vacancies, lattice disruptions, etc. Due to annealing these defects are removed and the cell contracts. The dangling bonds on the ZnO surface interact with oxygen ions in the atmosphere and because of the electrostatic attraction, this leads to a lattice that is slightly contracted [36]. For the $ZnAl_2O_4$ phase, the position of the (311) peak is shifted towards the lower angles reflecting an increase in the interplanar lattice spacing d_{hkl} which induces a strain between the (hkl) atomic planes where the lattice constant *a* increases. The slight increase of the crystalline parameter of zinc aluminate is 0.808 nm. Kaur et al. reported that the intrinsic stress is induced by the deposition parameters such as growth temperature and the deficiency of crystallites during the growth can allocate this intrinsic stress [37]. The surface disorder in the nanoparticles is due to the annihilation of chemical bonds and oxygen vacancies at different sub-lattice on the surface [38]. With the decrease in the size of the nanoparticles, the surface disorder becomes more pronounced (more atoms are on the surface than in the center because of the large surface area to volume ratio of small nanoparticles) [38]. Rusu et al. observed that the ZnO residual stress became compressive from a tensile one by the annealing at high temperature leading to the improvement of the film crystallinity [32].

The chemical composition of the nanostructured film is given in figure 2. The EDX spectrum shows the typical emission lines of the oxides principal constituent elements mainly zinc (ZnL), aluminum (AlK) and oxygen (OK). On the other hand, the appearance of silicon (SiK) and oxygen (OK) peaks comes from the SiO_2 coated glass substrate. The presence of impurities Ca and Cl comes from specimen preservation/transport and salt precursor.

Due to the high content of Zn and Al which is attributed to the film thickness and because the film and the glass substrate contain oxygen, the stoichiometry of the film is measured only from the Al and Zn signals.

The theoretical weight percent of $ZnO/ZnAl_2O_4$ films considering only Zn and Al is 29.22% Al and 70.78% Zn. The experimental results of the massic percentages of $ZnO\&ZnAl_2O_4$ films are summarized in Table 2.

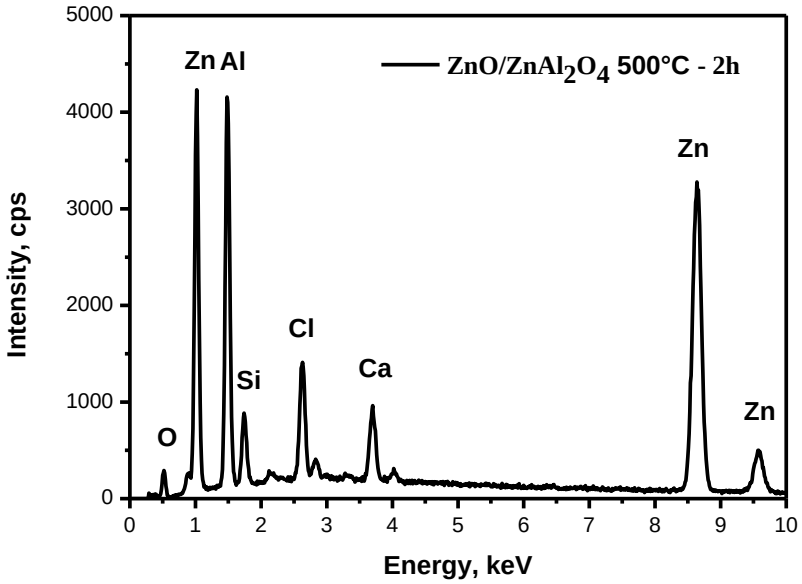

Fig. 2. EDX spectrum of $ZnO\_ZnAl_2O_4$/glass film with Zn/Al molar ratio equal to 0.07/0.13 (R_1).

Table 2. Massic percentages C of Zn and Al elements, of ZnO and $ZnAl_2O_4$ and volume fractions in the ZnO_$ZnAl_2O_4$ composite film deposited on glass substrate.

Annealing temperature	Zn/Al Molar ratio concentrations	Element	C, %	f_{ZnO}	$f_{ZnAl_2O_4}$	ZnO/$ZnAl_2O_4$	
						Weight% of $ZnAl_2O_4$	Weight% of ZnO
500°C	0.07/0.13	Zn Lα	63.41	0.276	0.724	74.0	26.0
		Al Kα	35.56				

The following expression is used to calculate *fi* (volume fraction of the i phase) from the concentration:

$$C_{Zn\ dans\ ZnO} = \frac{C_{Zn\ dans\ ZnO\ /\ ZnAl2O4}}{2} = \frac{\rho_{ZnO} \times V_{ZnO}}{\rho_{ZnO} \times V_{ZnO} + \rho_{ZnAl2O4} \times V_{ZnAl2O4}} \quad (11)$$

$$C_{Zn\ dans\ ZnO} = \frac{\rho_{ZnO} \times f_{ZnO}}{\rho_{ZnO} \times f_{ZnO} + \rho_{ZnAl2O4} \times f_{ZnAl2O4}} \quad (12)$$

where ρ_i is the density of constituent *i*, and f_i is the volume fraction of constituent *i* with $f_{ZnO} = V_{ZnO} / V_t$ $f_{ZnA2O4} = V_{ZnAl2O4} / V_t$, $f_{ZnA2O4} + f_{ZnO} = 1$ and V_t is the total volume. The densities reported for ZnO and $ZnAl_2O_4$ were used (ρ_{ZnO} = 5.61 g/cm^3 et $\rho_{ZnAl2O4}$ = 462 g/cm^3).
It is evident that the analyzed film consists of the ZnO and $ZnAl_2O_4$ composite oxides.

Vibrational spectroscopies are widely used techniques to characterize materials because they are nondestructive, noninvasive tools that provide information about the molecular composition and structure. These two analytical techniques, namely, infrared and Raman spectroscopy, measure vibrational energy levels which are associated with the chemical bonds in the sample [39]. The FTIR spectrum of the deposited film onto glass substrate heat treated at 500°C during 2 h in figure 3 indicates the formation of zinc oxide and zinc aluminate. Metal-oxygen bands observed in the range of 400 to around 700 cm^{-1} are characteristic to ZnO and $ZnAl_2O_4$. The sharp absorption peaks located at 505, 551 and 662 cm^{-1} are assigned to the regular spinel structure with octahedrally coordinated aluminum centers only [31, 20]. The 662, 551 and 505 cm^{-1} frequencies are related to the vibrations of Al–O symmetric stretching vibration (ν_1), Al–O symmetric binding vibration (ν_2) and Al–O asymmetric stretching vibration (ν_3),respectively [20, 40]. Zn–O stretching mode in ZnO structure is centered at about 420 cm^{-1} and red shifted compared with that of bulk material (437.33 cm^{-1}), previous researchers found the IR ZnO band between 419 and 464 cm^{-1} [31, 41, 42, 43]. Bands formed at about 1632, 1385 and 1031 cm^{-1} are due to the H-O-H bending vibration of adsorbed water [20], C=O stretching mode of acetate precursor salt (metal vibration modes attached to hydroxyl groups) [41] and the deformation vibrations of Si-O (glass) [44], respectively. The small peak at 1055 cm^{-1} represents C=O deformation [43]. The FT-IR and XRD results are in good agreement to confirm ZnO and $ZnAl_2O_4$ semiconductors formation in the glass supported film. However, according to Fang et al. the IR data of Zn spinel are complex, authors reported that an IR vibrational transverse optic (TO) value at around 750 cm^{-1} (shoulder, broad) of the gahnite can be detected [45].

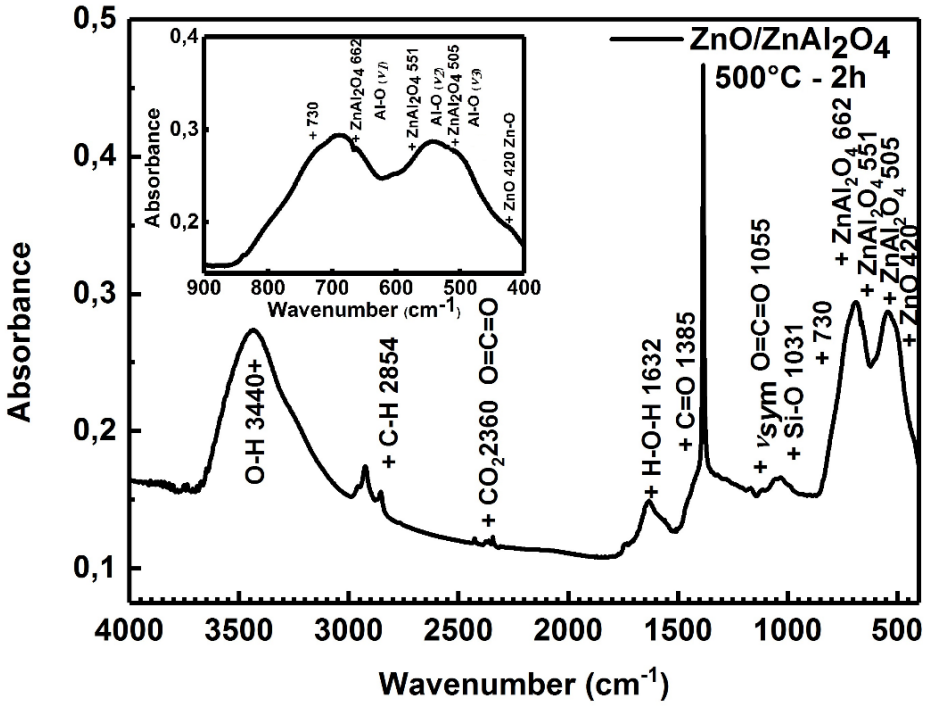

Fig. 3. FTIR pattern of ZnO_$ZnAl_2O_4$ composite oxides film, exhibiting the presence of ZnO and $ZnAl_2O_4$ vibration bands.

It should be mentioned that when the Zn and Al molarities decreases ~ 0.035/0.065, the film coated on the glass substrate in practically the same other deposition conditions and annealing at 500°C temperature, exhibits zinc oxide single phase as it is shown in figure 4.

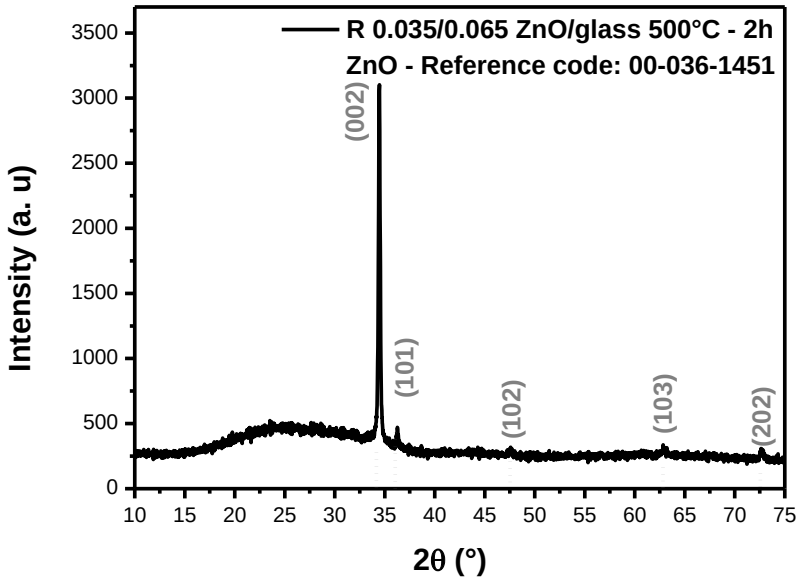

Fig. 4. XRD pattern of ZnO thin film deposited with Zn to Al molar ratio of 0.035/0.065 annealed at 500°C-2h, crystallization of ZnO as a single phase.

Figure 5 shows the optical transmittance spectrum of ZnO/$ZnAl_2O_4$ film deposited on glass substrate. The solid curve in fig. 5 corresponds to the curve fitting using optical model described in previous work [46], and the symbol represents the experimental data. The figure shows a good reasonable fit to the experimental data, which implies a precise determination of the optical parameters *d*, E_g, , rms and listed in table 3. By applying Levenberg-Marquardt least-square method, the experimental transmittance data (T_{exp}) were fitted completely with the transmittance data

calculated (T_{theo}) via a combination of Wemple-Didomenico model, absorption coefficient of an electronic transition (or charge-transfer transition) and Tauc-Urbach model [46]. Minimizing a sum of squares generated for different values of the thickness (d) and wavelength of gap (λ_g) by iterative technique and finding the corresponding refractive index (n) and extinction coefficient (k), the exact film thickness and energy gap can be calculated [46].

The ZnO/$ZnAl_2O_4$ film exhibited a transparency of around 60 % in the visible (400-800 nm) and the near infrared (800-1100 nm) regions. The ultraviolet cutoff in transmission for wavelengths around 380 nm corresponds to the intrinsic absorption in ZnO due to electron transitions between the valence band and the conduction band ($O_{2p} \rightarrow Zn_{3d}$) [47]. The absorption edge with a shoulder at around 320 nm in the near UV is associated with the absorption edge in $ZnAl_2O_4$. The band gaps of both oxides were evaluated based on the Tauc relation [48] by plotting versus and extrapolating the linear part of the plot to $h\upsilon$ axis (x axis) (see supplementary Fig. 6):

$$\alpha(\upsilon) = \frac{\alpha_0 (h\upsilon - E_g)^n}{h\upsilon} \tag{13}$$

where α is absorption coefficient and estimated from $\alpha = 2.303 \log (T/d)$, T is the transmittance, d is the film thickness, α_0 a constant, E_g is the band gap, is the photon energy, eV is the unit for band gaps and exponent n depends on transition type (n = 1/2 for direct allowed.

The energy value of the ZnO band gap is in perfect agreement with those already announced by other authors ($E_g = 3.24 \pm 0.10$ eV) [46, 49] and remain close to that of massive ZnO 3.3 eV [50]. USP technique can prove its performance compared to physical deposition techniques. The E_g of polycrystalline zinc aluminate is between 3.8 - 3.9 eV [51], the value of the gap of $ZnAl_2O_4$ in our film are very close to this energy range. Bouzid et al. reported that the compression stress causes an increase in band gap, which corresponds perfectly to the correlation between E_g and the stress of zinc aluminate film [43]. The decrease in E_g is also due to the reduction in the state density of charges, Letailleur et al. in ZnO reported a similar result in ZnO: Al films [52]. The $ZnAl_2O_4$ E_g increases after thermal annealing, this is attributed to the improvement of its crystallinity and structural reorganization, (for example with the disappearance of dangling bonds or impurities in the material) [31] and therefore increasing grain size. From UV-Vis transmittance analysis, the estimated refractive index at 598 nm and the root-mean-square (rms) surface roughness of 0.07/0.13: ZnO/$ZnAl_2O_4$/glass thin film are 1.7 and 52 nm respectively. The composite thin film refractive index value is in good agreement with that of $ZnAl_2O_4$ 1.79 [53] and (n ZnO: 1.81-1.91) [43], and slightly lower than that of solid ZnO 2.0 [54]. Generally, n ZnO thin film decreases with the regime of long wavelength and after the incorporation of Al in the ZnO matrix [31].

The XRD profiles of Si(100) and Si(111) supported annealed films are given in fig. 7(a) and 7(b), respectively. From the figure 7(a) it is noticed that some diffraction peaks agree well with the standard pattern of ZnO phase (JCPDS card No. 36-1451), reflecting the (002) and (101) planes. No diffraction peaks are assigned to Al and a very minor diffraction peak intensity can be ascribed to the (004) plane of spinel $ZnAl_2O_4$ structure has appeared (JCPDS card No. 01-073-1961), which ensures that Al acetate decomposes completely into products after annealed at 500°C for 2 hours in air. The residual $ZnAl_2O_4$ phase is in a very weak crystalline nature. The main crystal phase was in *willemite* α-Zn_2SiO_4 by the diffraction of a series of sharp and intense peaks. The peaks position are found well matching with those of the standard pattern of α-Zn_2SiO_4 (Rhombohedral crystal structure with an R3 space group, lattice parameters, a = b = 13.9381 (Å) and c = 9.3100 (Å), JCPDS card No. 37-1485). Babu et al. have found, on the synthetized of doped Zn_2SiO_4 phosphors by sol-gel method that the nucleation temperature of non-crystalline SiO_2 and *willemite* β-Zn_2SiO_4 crystalline phase is between 700 and 800°C [55], when the calcination temperature increases to 900 and 1000°C the full crystallization of *willemite* α-Zn_2SiO_4 at the expense of ZnO occurred [55]. Xu et al. have fabricated zinc silicate/silica ZnO nanowires (by a chemical vapor deposition route) reported that the ZnO–SiO_2 system around 800°C is easily transformed into a mixed phase including a hexagonal ZnO, a tetragonal Zn_2SiO_4 and an amorphous SiO_2 [56]. From the chemical reaction dynamics point of view,

the following reaction may occur at the interface of ZnO/SiO_2 under the circumstance of a higher silica concentration: $2ZnO + SiO_2 \rightarrow Zn_2SiO_4$ [56]. Probably a layer of the silicon oxide was formed during annealing and reacts with zinc oxide to form zinc orthosilicates. From the XRD diagram of the figure 7(b), it can be seen that film contains the two phases ZnO and $ZnAl_2O_4$ according to JCPDS, 36-1451and 01-073-1961, respectively. Seven peaks at 31.90°, 34.60°, 36.38°, 47.67°, 56.79°, 63.1° and 72.88° coincide with ZnO (100), (002), (101), (102), (110), (103) and (004) planes. Additionally, the Si(111) peak positioned at 28.53° was detected. When the Zn concentration increases to 0.1 and the substrate became Si(111), the intensity of the ZnO (002) peak became higher and sharper. The observation of the strong ZnO (002) peak compared to the neighboring ZnO peaks indicates that the highly *c*-axis oriented ZnO/Si(111) film was grown. Furthermore, it can be allowed that the ZnO crystallinity improves progressively with increasing the concentration of Zn to Al and with Si(111) substrate. The ZnO crystallites size grown onto Si(111) and Si(100) were 57 nm and 28 nm, respectively (see table 4). Ali et al. have studied the Si(111) supported $ZnO-SiO_2$ thin films annealed at different temperatures prepared by sol-gel [57]. They reported that the relative intensity of the ZnO (100) diffraction line compared to the other lines was increased by increasing the annealing temperatures and ZnO concentration to SiO_2. The diffraction peak depicted at 31.16° with relatively important intensity belongs to the spinel $ZnAl_2O_4$ (220) plane. Thereby, with an increased of the Zn concentration and the used of Si(111)-oriented single crystal substrate the formation of zinc silicate remains suppressed and a mixed of high crystalline zinc aluminate $ZnAl_2O_4$ and zinc oxide ZnO has been obtained. However, these conditions of 0.1/0.1 Zn to Al molar ratio and the Si(111) substrate are appropriate to the nucleation of the corundum α-Al_2O_3 phase by the appearance of a minor peak at 25.71° associated to the (012) plane according to the standard pattern (rhombohedral crystal system with space group, lattice parameters, a = b = 4.7580 (Å) and c = 12.9910 (Å), JCPDS card No. 10-0173). The α-alumina phase can be considered as an impurity compared to the major ZnO and $ZnAl_2O_4$ structures [21]. From, these observations of XRD profiles reveal that the Si(111) substrate is more suitable than Si(100) for the growth of $ZnO/ZnAl_2O_4$ film and that the Zn/Al ratio molarities (~ 0.1/0.1) is also an important factor for the facile formation and growth of high crystalline $ZnO/ZnAl_2O_4$ nanocomposite.

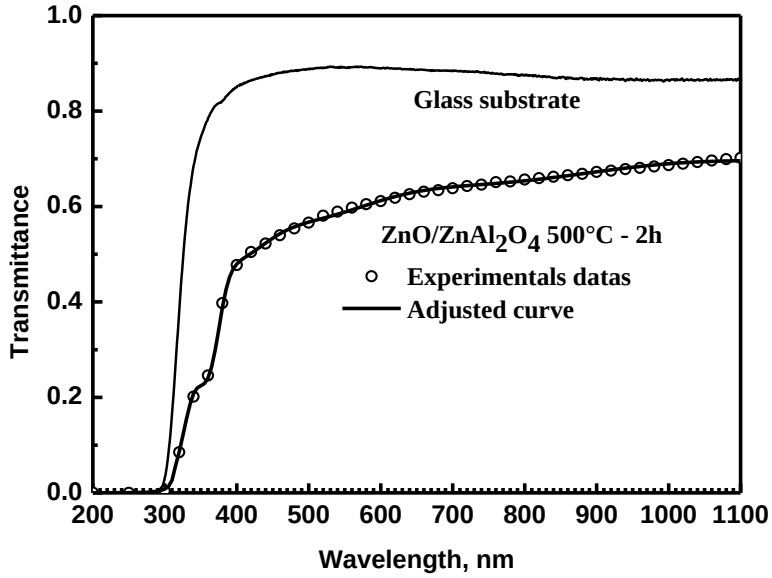

Fig. 5. Superposition of theoretical and experimental transmittance curves of $ZnO\_ZnAl_2O_4$ film on glass substrate with Zn/Al molar ratio equal to 0.07/0.13.

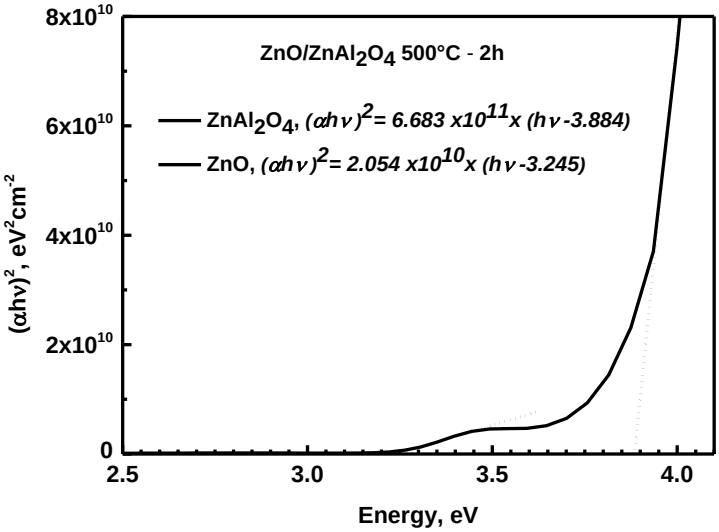

Fig. 6. Versus energy spectrum for ZnO_$ZnAl_2O_4$ film on glass substrate with dashed line showing the extrapolation for zero absorption (x-axis intercept represents the optical band gap).

Table 3. Dispersion parameters of film obtained by adjustment of experimental dates.

$ZnO/ZnAl_2O_4$/glass T, annealing	Thickness, (nm)	E_g, (eV)	*n* à 598 nm	n_∞	rms, (nm)
500°C	377	ZnO : 3.245 $ZnAl_2O_4$: 3.884	1.744	1.700	52

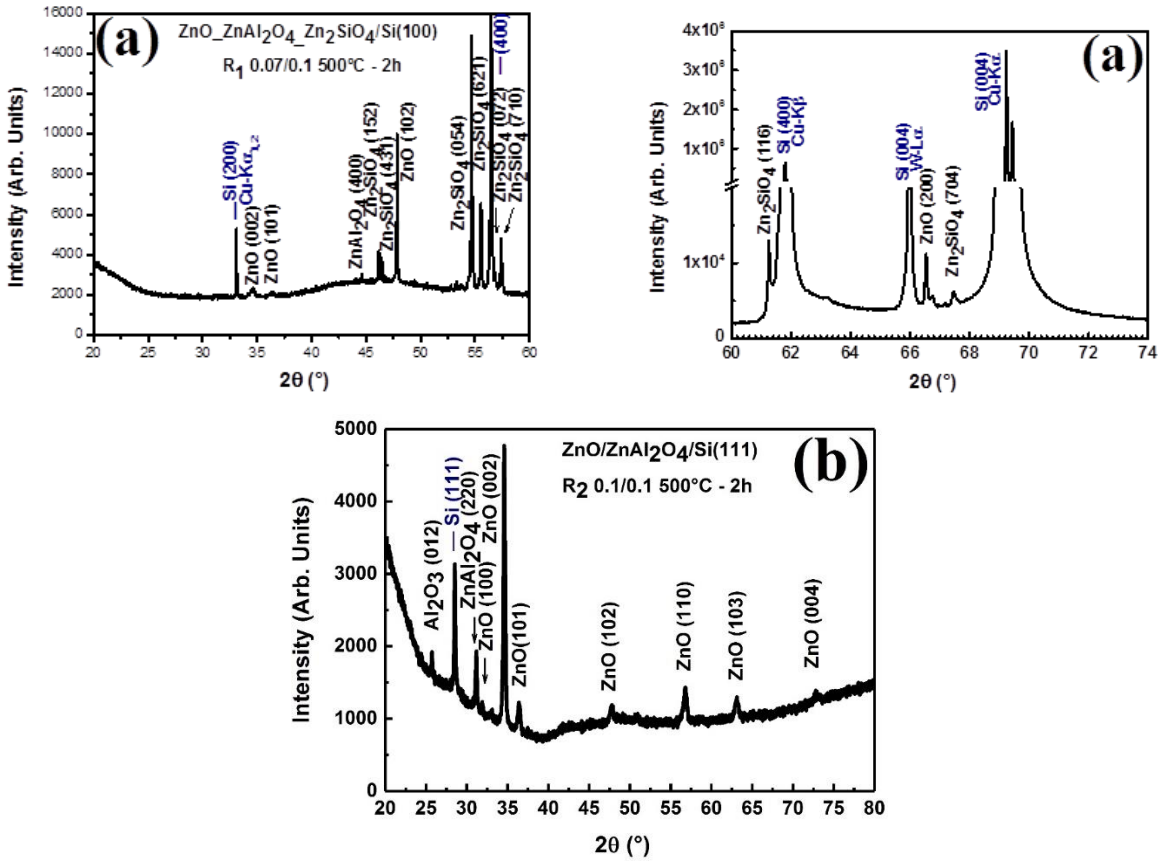

Fig. 7. X-ray diffraction spectra of the ZnO_$ZnAl_2O_4$ films deposited with Zn to Al molar ratio of (a) 0.07/0.13 on Si(100) and (b) 0.1/0.1 on Si(111): improvement in the purity and crystalline quality of the composite. (ZnO, $ZnAl_2O_4$, Zn_2SiO_4 and Si(111) JCPDS, 36-1451, 01-073-1961, 37-1485 and 03-0549, respectively).

Table 4. The XRD datas of the $ZnO/ZnAl_2O_4$ films deposited on Si substrate.

Film $ZnO/ZnAl_2O_4$	Pos. [°2Th.]	FWHM [°2Th.]	Identified Plans (h k l)	d_{hkl} (Å)	Size of crystallites *D* [nm]
	34.590	0.312	002 ZnO	2.465	28
R_1 = 0.07/0.13 0.5 on Si(100)	44.611	0.094	400 $ZnAl_2O_4$	2.03	89
R_2 = 0.1/0.1	34.602	0.154	002 ZnO	2.592	57
1 on Si(111)	31.162	0.077	220 $ZnAl_2O_4$	2.870	108

Zinc aluminate with spinel structure, according to group theory analysis, should exhibit five normal Raman active modes of vibration $A_{1g}(R) + Eg(R) + 3T_{2g}(R)$ [58, 59, 60]. Generally, the mode frequencies keep the sequence $T_{2g}(1)<Eg<T_{2g}(2)<T_{2g}(3)<A_{1g}$ [60]. One of the weakest modes is T_{2g} mode with the lowest frequency. For the zinc oxide with hexagonal wurtzite structure C_{6v} ($C6_3mc$) symmetry, the group theory predicts for the optical phonons at the point of Brillouin zone the following representation: $= 1A_1 + 1E_1 + 2E_2 + 2B_1$ [61, 62, 63, 64]. The first-order Raman active modes are A_1 (574 and 380 cm^{-1}), E_1 (583 and 407 cm^{-1}) and E_2 (101 and 437 cm^{-1}) (associated with theoretical frequencies), and B_1 remains silence [61, 62, 65]. There are several frequencies longitudinal optical (LO) and transversal optical (TO) components for the polar modes A_1 and E_1 [63]. E_2 mode consists of low and high basic phonons modes [66].

Silicon supported nanocomposite films Raman spectra were collected over the range 100-900 and 50-900 cm^{-1} (Fig. 8) for Si(111) and Si(100) substrates, respectively, in order to further confirm the existing of second or other third phases. The Raman signals are very sensitive to the crystal structure as well as to the defects embedded in. The peaks at about 300(303), 524(527), and 617(620) cm^{-1}, respectively, on figure 8(b) and (fig. 8(a)) were due to scattering from the silicon substrates [67]. The main phonon mode is the fingerprint of wurtzite crystal structures [68] and is related to the crystalline nature, phase orientation and strain present in the ZnO matrix [67]. The sharp and dominant peaks at 434 and 435 cm^{-1} are attributed to the high-E_2 of nonpolar optical phonons of ZnO nanostructures grown on Si(111) and Si(100) substrates, respectively. The mode is commonly detected in the wurtzite structure ZnO and is a characteristic one [61, 62]. The high-E_2 intrinsic Raman active mode is associated with the oxygen motion [61]. The intensity of the peak at 434 cm^{-1}, figure 8(b) as compared to other peaks is relatively high, which indicates that the residual stress had reduces leading to the high crystal quality of zinc oxide grown over Si(111) orientation with Zn/Al_0.1/0.1 molar ratio [68, 64], and is a very sharp feature. This result is consistent with XRD. The 435 cm^{-1} high-E_2 mode, (fig. 8(a)), is also the slightly most intense to the other observed peaks (with the exception of the silicon peaks) but with the broadening of the band which may suggest larger lattice distortion of Si(100) supported ZnO nanostructure with 0.07/0.13 relatively low molar ratio. The high crystal quality of ZnO/Si(111) film is supported by the appearance of the well-defined 575 cm^{-1} A_1 (LO) first-order phonon peak, (see fig. 8(a)), Lupan et al. reported that the A_1 (LO) band becomes stronger only in the ZnO structure with higher crystallinity [62], and according to Kunj et al. the E_2 and A_1 (LO) are the only allowed modes for backscattering along the preferred *c*-axis of the crystal [65]. The A_1 (LO) is connected to the resonance of exciting phonon energy with that of electronic inter band transition within the ZnO [69]. The 99 cm^{-1} low-E_2 mode which is a fundamental phonon mode is detected in the ZnO structure coated on Si(100) support according to the figure 8(a). The mode involves the vibration of the Zn sublattice [65, 70]. It is worth noting that low-E_2 mode is red-shifted (until -5 cm^{-1}), in general for different ZnO morphologies as reported by Khan [68]. The band was not visible on the spectrum of figure 8(b), because the analysis was recorded from 100 cm^{-1}. A smaller peak at 409 cm^{-1} is attributed to E_1 (TO) phonon mode associated with lattice disorder along the c-axis of the ZnO crystal modes [64], the defect change caused by O-vacancy, Zn-interstitial states or their complexes and free carriers are respond to the presence of E_1 (TO) mode [64, 61, 66]. According to this observation, *w*-ZnO thin film deposited on Si(100) wafer exhibited a low structural quality. It is interesting to note that from ZnO grown on Si(111) wafer with 0.1/0.1

higher molarities, E_1 (LO) multiphonon does not appear. The shift in the mode position informs about the nature of residual stress present in the film, when the (437 cm^{-1}) line is reported towards the higher/lower wavenumber it corresponds to a compressive/tensile stress in the ZnO structure [65]. Our ZnO/Si films are under a tensile stress. As the XRD of Si supported films (fig. 7) exhibited growth along different planes, contribution from additional Raman modes due to grains disoriented from (002) crystal plane was expected [65]. The peaks position at 439 and 470 cm^{-1} are assigned to A_{1g}, $_{v2}(SiO_4)$ mode and the bending vibrations of SiO_4 group, respectively of zinc silicate Zn_2SiO_4 for nanocomposite film deposited on Si(100) substrate [23, 71]. The spectrum (fig. 8(a)) possess phonon frequencies at 826 and 451 cm^{-1}, which are associated to Si-O and SiO_2 modes, respectively [72], suggesting the formation of silicon dioxide layer on the substrate.

Comparing the ZnO nanoparticles with molarities (0.07/0.13) on Si(100) and (0.1/0.1) on Si(111), (Fig. 8(a) and (b)) respectively, the intensity of mode increased with increasing Zn concentration and processing deposition on Si(111). The ZnO/Si(111) film is characterized also by:

- The appearance of a basic phonon 381 cm^{-1} A_1 (TO) mode practically unshifted, (see fig. 8(b)) [64, 62, 66]. The peak at around 321 cm^{-1} is assigned to the - multiphonon scattering [70].
- Disappearance of SiO_4 modes, fig. 8(a) with increasing Zn salt concentration and using Si(111) substrate. The intensity of 825 cm^{-1} Si-O band decreased, figure 8(b).

D'Ippolito et al. in 2015 have investigate a study on oxide spinels to identify Raman peculiarities of each end-member and clarify how substitution of the divalent and trivalent cations affects the Raman modes [59]. The authors stated that each spinel end-member exhibits a Raman fingerprint with at least one peculiar peak in terms of Raman shift and relative intensity. The $ZnAl_2O_4$ spinel end-member exhibits an intense $T_{2g}(3)$ mode and a low or absent A_{1g} mode. Three Raman modes of the five Raman-active modes of the spinel phase were recorded on the gahnite ($ZnAl_2O_4$), they are the E_g mode at 420.6 cm^{-1} due to Zn in ZnO_4 tetrahedra, and the $T_{2g}(2)$ 510 cm^{-1}, the $T_{2g}(3)$ mode at 661 cm^{-1}, due to Al in AlO_6 octahedra [58], what is reported is in excellent agreement with our result. The recorded spectra of the 0.07/0.13 and 0.1/0.1 molarities on Si(100) and (111) substrates, respectively (Fig. 8(a) and (b)) show two Raman active modes at 421 and 671 cm^{-1} for Si(100) supported film and 417 and 663 cm^{-1} for Si(111) supported one. The observed 421 and 417 cm^{-1} peaks are assigned to $ZnAl_2O_4$ E_g mode and the 671 and 663 cm^{-1} frequencies to $ZnAl_2O_4$ T_{2g}, these features are in agreement with the previous measurements and calculations from the literature [59, 58]. Table 5. summarizes the theoretical and experimental Raman modes of zinc aluminate; our recorded peaks are strongly consistent with reported data on $ZnAl_2O_4$. The $ZnAl_2O_4$ 417 cm^{-1} E_g band, fig. 8(b) is well separated from the 435 cm^{-1} high-E_2 mode and more narrow than on fig. 8(a). Also, the 517 cm^{-1} Si band, fig. 8(b) is asymmetric and larger than the FWHM of standard peak (~ 3 cm^{-1}) [75] which suggests the supporting of the $ZnAl_2O_4$ 511 cm^{-1} $T_{2g}(2)$ mode with very low intensity comparing to Si–Si one (the frequencies of the two peaks are very close and their arbitrary intenties very different).

The representation of optical modes in α-Al_2O_3 by D_{3d}^6 symmetry analysis using group theory is given as:

$$\Gamma = 2A_{1g} + 2A_{1u} + 3A_{2g} + 3A_{2u} + 5E_g + 5E_u \quad (14)$$

Among these, two A_{1g} and five E_g modes are Raman actives [76, 77]. Therefore, corundum (α-alumina) gives rise to seven Raman active modes [76, 77]. According to the spectrum of the figure 8(b), the Raman active modes of α-alumina have a weak presence. The presence of a minor phase α-Al_2O_3 is suggested by the formation of weak bands corresponding to the E_g (external) (392 cm^{-1}) and A_{1g} (403 cm^{-1} and 634 cm^{-1}) [76, 77]. Additionally, Raman peak position at 683 cm^{-1} is originated from the acetate groups used as an Al reactant in the synthesis process, and attributed to the O-C-O symmetric band [66].

Figure 9 shows the room temperature Raman spectrum of the ZnO/$ZnAl_2O_4$ glass coated film (using a solid-state laser (532 nm)). The depth penetration is more important (~ 400 nm), fewer peaks relating to metal oxides are recorded and their intensity is affected. ZnO and $ZnAl_2O_4$ nanoparticles

are present, showed some usual modes that were observed at 104 cm^{-1} (corresponding to the ZnO E_2 (low) mode), 590 cm^{-1} (ZnO E_1 (LO)), 659 cm^{-1} (E_2 (low) + B_1 (high)) [64], 553 cm^{-1} ($ZnAl_2O_4$ $T_{2g}(2)$) and 663 cm^{-1} ($ZnAl_2O_4$ $T_{2g}(3)$), respectively [59]. The peak at 561 cm^{-1} corresponds to the glass in comparison with the spectrum recorded on the substrate (spectrum not reported).

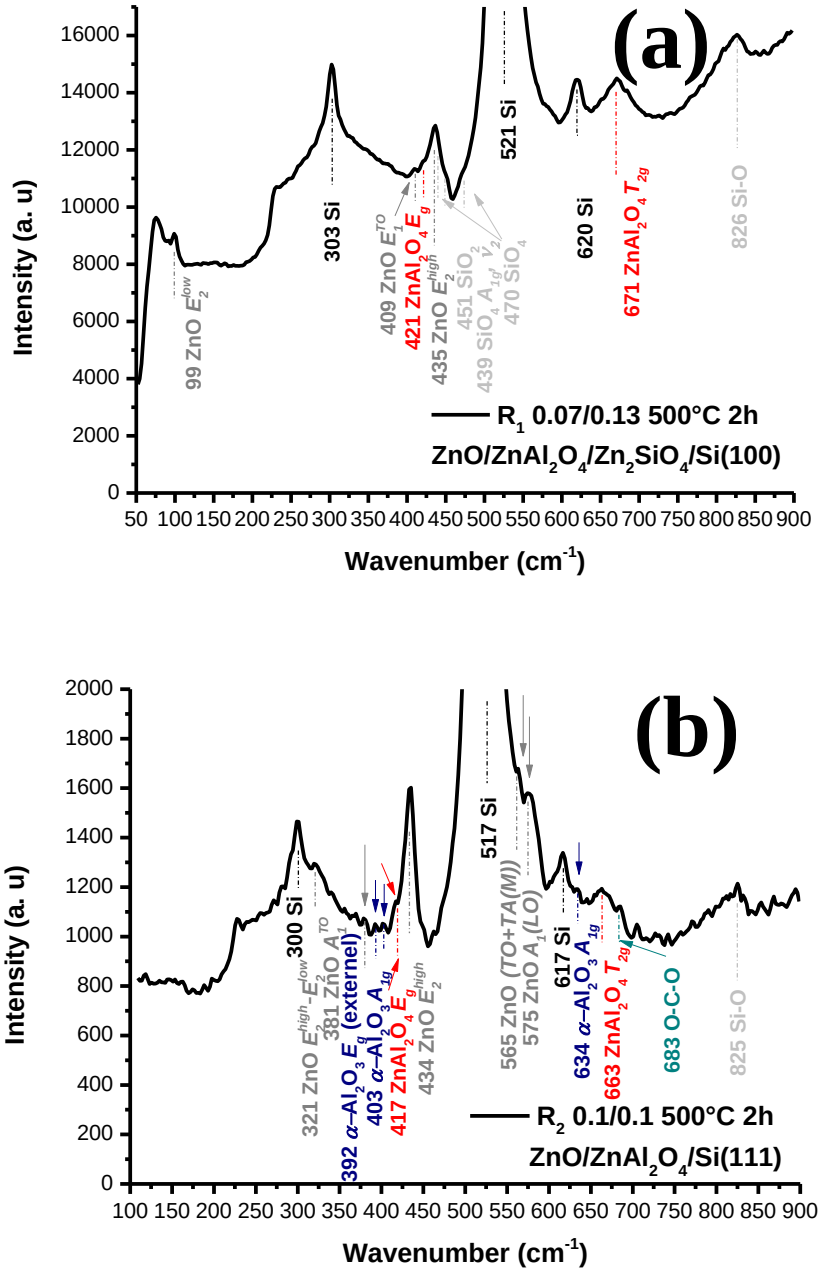

Fig. 8. Micro-Raman patterns of films: (a) ZnO_$ZnAl_2O_4$ _ Zn_2SiO_4/Si(100) and (b) ZnO_$ZnAl_2O_4$/Si(111) with R_1 = 0.07/0.13 and R_2 = 0.1/0.1, respectively.

Table 5. Theoretical and experimental frequencies (in cm^{-1}) for the Raman modes of the cubic spinel structure $ZnAl_2O_4$.

Modes	$T_{2g}(1)$	E_g	$T_{2g}(2)$	$T_{2g}(3)$	A_{1g}
Fang et al. 2002 [45] Theory	194	442	520	665	784
López-Moreno et al. 2011 [73] Theory	197	427	513	655	775
D'Ippolito et al. 2015 [59] Experiment		411	510	661	
D'Ippolito et al. 2013 [58] Experiment		420	510	661	
Chopelas et al. 1991 [74] Experiment	196	417	509	658	758
Iaiche et al. 2020 This work Experiment		417	511	663	

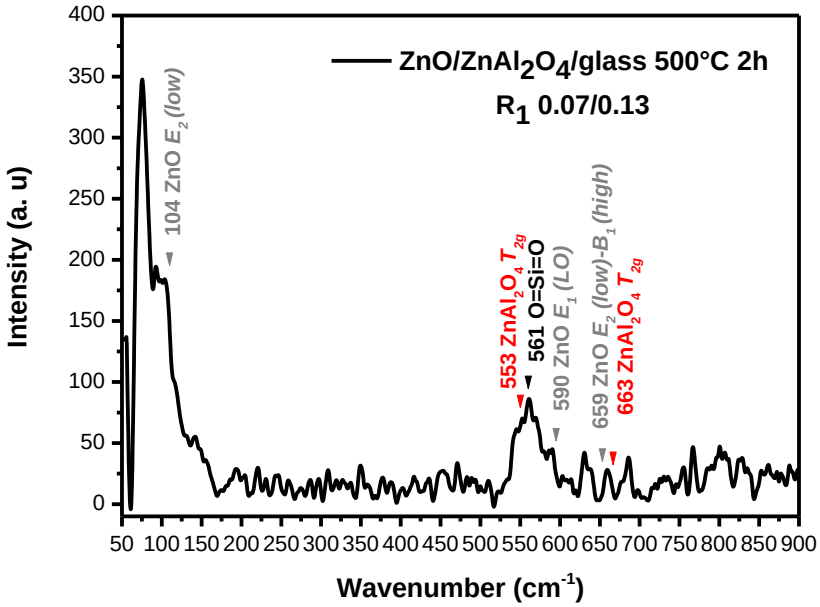

Fig. 9. RT Micro-Raman spectrum of ZnO_$ZnAl_2O_4$ sample deposited on glass substrate with R_1 molar ratio of 0.07/0.13.

4. Conclusion

The ZnO-$ZnAl_2O_4$ films onto 450 °C heated glass and silicon substrates are obtained by a simple ultrasonic spray pyrolysis synthesis process. The formation control of nanocomposites oxides is verified accurately- by XRD, Raman and FTIR spectroscopy. The effect of zinc and aluminum molarities on the ZnO and $ZnAl_2O_4$ oxides crystalline quality is discussed. The Zn/Al molar ratios of about 0.07/0.13 and 0.1/0.1 leaded to the growth of high crystalline ZnO-$ZnAl_2O_4$ layers onto glass and Si(111) substrates, respectively. The film grown onto Si(100) substrate with Zn less content (0.07 M) is attributed to the multifunctional Zn_2SiO_4-ZnO-$ZnAl_2O_4$ materials. Zn_2SiO_4 principal phase is well crystalline than ZnO and $ZnAl_2O_4$ oxides. The lower Zn/Al molar ratio around 0.035/0.065 produced only ZnO single phase onto glass and is inadequate for the formation of ZnO-$ZnAl_2O_4$ system. The crystallinity of the prepared samples was analyzed by X-ray diffraction and by Raman spectroscopy induced upon annealing at 500°C for 2 hours in the ambient. The obtained ZnO

films exhibited a preferential (002) orientation with perpendicular *c*-axis of hexagonal wurtzite structure. The *TC(hkl)* value indicated that $ZnAl_2O_4$ in the ZnO/$ZnAl_2O_4$/glass layer is polycrystalline preferentially oriented along the (311) plane. Spinel $ZnAl_2O_4$ oxide onto Si(111) substrate grown according to the (220) orientation. The Raman spectrum of Si(111) supported film is dominated by the vibrational modes expected to the ZnO wurtzite structure with the appearance of the basic phonon 381 cm^{-1} A_1 (TO) mode comparatively to Si(100) supported layer analysis. The ZnO and $ZnAl_2O_4$ nonmetric crystallites size grown on Si are much higher than those on glass. The estimated crystallites size and stress values of the ZnO and $ZnAl_2O_4$ in the ZnO/$ZnAl_2O_4$/glass film were 19 nm/0.469 GPa and 11 nm/-0.292 GPa, respectively. The spray process was specific: continuous, with a low flow rate and for an extended time around 03 hours for giving enough energy for oxides particles or germs to better coalescence. The employed annealing temperature is relatively low for the obtained high crystalline quality of $ZnAl_2O_4$ oxide. Results from UV-visible spectroscopy provide an overview of the ZnO and $ZnAl_2O_4$ E_g values dependent on Zn and Al content on glass substrate. The ZnO/$ZnAl_2O_4$ film is transparent in the visible and near infrared regions and highly sensitive to UV absorption indicating that they are suitable for UV applications photoconductive sensor and gas sensors.

References

[1] M. Shahmirzaee, M. Shafiee Afarani, A. Masoud Arabi, A. Iran Nejhad, In situ crystallization of $ZnAl_2O_4$/ZnO nanocomposite on alumina granule for photocatalytic purification of wastewater, Res. Chem. Intermed. 43 (2017) 321–340.

[2] Y. Jianhui, Z. Li, L. Xiaoyan, Z. Xiuxiu, D. Chaohua, Preparation and Photocatalytic Properties of ZnO/CuO/$ZnAl_2O_4$ Composite Hollow Microspheres by One-Pot Method, Chem. Sci. Rev. and Lett. 3: 12 (2014) 1080-1090.

[3] L. Zhang, J.Y. Minjie Zhou, Y. Yang, Y-N. Liu, Fabrication and photocatalytic properties of spheres-in-spheres ZnO/$ZnAl_2O_4$ composite hollow microspheres, App. Sur. Sci. 268 (2013) 237-245.

[4] X. Yuan, X. Cheng, Q. Jing, J. Niu, D. Peng, Z. Feng and X. Wu, ZnO/$ZnAl_2O_4$ Nanocomposite with 3D Sphere-Like Hierarchical Structure for Photocatalytic Reduction of Aqueous Cr(VI), Mater. 11, (2018) 1624-1647.

[5] K. Kumar, K. Ramamoorthy, P-M. Koinkar, R. Chandramohan, K. Sankaranarayanana, J. Cry. Gro. 289 (2006) 405-407.

[6] R. Huo, y. Kuang, Z. Zaho, F. Zhang, S. Xu, Enhanced photocatalytic performances of hierarchical ZnO/$ZnAl_2O_4$ microsphere derived from layered double hydroxide precursor spray dried microsphere, J. Col. Inter. Sci. 407 (2013) 17-21.

[7] V. Kumari and A. Bhaumik, Mesoporous $ZnAl_2O_4$: an efficient adsorbent for the removal of arsenic from contaminated water, Dalt. Trans. 26: 44 (2015) 11843-11851.

[8] L. Zhang, J-h. Yan, M-j. Zhou, Y-p. Yu, Y. Liu, Y-n. Liu, Photocatalytic degradation and inactivation of *Escherichia coli* by ZnO/$ZnAl_2O_4$ with heteronanostructures, Transactions of Nonferrous Metals Society of China, 24: 3 (2014) 743-749.

[9] X.F. Zhao, L. Wang, X. Xu, X.D. Lei, S.L. Xu, F.Z. Zhang, Fabrication and photocatalytic properties of novel ZnO/$ZnAl_2O_4$ nanocomposite with $ZnAl_2O_4$ dispersed inside ZnO network, AIChE J. 58 (2012) 573–582.

[10] B. Behera, S. Pal, L. Kanungo, S. Bhand, S. Chandra, Synthesis and characterization of ZnO-$ZnAl_2O_4$ whiskers and their application in biosensors, J. Nan. Let. 5: 2 (2015).

[11] M-Y. Guan, D-M. Xu, Y-F. Song, Y. Guo, ZnO/$ZnAl_2O_4$ prepared by calcination of ZnAl layered double hydroxides for ethanol sensing, Sensors and Actuators B, 188 (2013) 1148-1154.

[12] M. Hoppe, O. Lupan, V. Postica, N. Wolff, V. Duppel, L. Kienle, I. Tiginyanu, R. Adelung, $ZnAl_2O_4$ - functionalized zinc oxide microstructures for highly selective hydrogen gas sensing applications, Physica Status Solidi (a), 215(7) (2018).

[13] R. Huo, y. Kuang, Z. Zaho, F. Zhang, S. Xu, Enhanced photocatalytic performances of hierarchical ZnO/$ZnAl_2O_4$ microsphere derived from layered double hydroxide precursor spraydried microsphere, J. Coll. Inter. Sci. 407 (2013) 17-21.

[14] Y.D. Ivakin, M.N. Danchevskaya, O.G. Ovchinnikova, G.P. Muravieva, Thermovaporous synthesis of fine crystalline gahnite ($ZnAl_2O_4$), J. Mater. Sci. 41 (2006) 1377–1383.

[15] J.L. Suárez-Franco, M. García-Hipólito, M.Á. Surárez-Rosales, J.A. Fernández-Pedrero, O. Álvarez-Fregoso, J.A. Juárez-Islas, and M.A. Álvarez-Pérez, Effects of Surface Morphology of $ZnAl_2O_4$ Ceramic Materials on Osteoblastic Cells Responses, Journal of Nanomaterials, (2013).

[16] M. García-Hipólito, C.D. Hernández-Pérez, O. Alvarez-Fregoso, E. Martıınez, J. Guzmaan-Mendoza, C. Falcony, Characterization of europium doped zinc aluminate luminescent coatings synthesized by ultrasonic spray pyrolysis process, Opt. Mater. 22 (2003) 345–351.

[17] H. Zhao, Y. Dong, P. Jiang, G. Wang, J. Zhang, C. Zhang, $ZnAl_2O_4$ as a novel high-surface-area ozonation catalyst : One-step green synthesis, catalytic performance and mechanism, Chemical Engineering Journal, 260 (2015) 623-630.

[18] P. Mierczynski, W. Maniukiewicz, T.P. Maniecki, Comparative studies of Pd, Ru, Ni, Cu/$ZnAl_2O_4$ catalysts for the water gas shift reaction, Cent. Eur. J. Chem. 11: 6 (2013) 912-919.

[19] E.L. Foletto, S. Battiston, J.M. Simoes, M.M. Bassaco, L.S. Fagundes Pereira, E.M. M. Flores, E.I. Muller, Synthesis of $ZnAl_2O_4$ nanoparticules by different routes and the effect of its pore size on the photocatalytic process, Micr. Meso.Mater. 163 (2012) 29-33.

[20] S-F. Wang, G-Z. Sun, L-M. Fang, L. Lei, X. Xiang & X-T. Zu, A comparative study of $ZnAl_2O_4$ nanoparticles synthesized from different aluminum salts for use as fluorescence materials, Scie. Rep. 5:12849 (2015.

[21] M.H. Mohd Zaid, K. Amin Matori, S.H. Abdul Aziz, H. Mohamed Kamari, Z. Abdul Wahab, Y. Wing Fen, I. Mustapha Alibe, Synthesis and characterization of low cost willemite based glass–ceramic for opto-electronic applications, J. Mater. Sci: Mater Electron, (2016).

[22] D. Kumar Bharti, M. Kumar Gupta, A. Kumar Srivastava, Giant dielectric constant and band gap reduction in hydrothermal grown highly crystalline zinc silicate nanorods, Mater. Lett. 232 (2018) 66–69.

[23] B. Chandra Babu, B. Vengla Rao, M. Ravi, S. Babu, Structural, microstructural, optical, and dielectric properties of Mn^{2+}:*Willemite* Zn_2SiO_4 nanocomposites obtained by a sol-gel method, J. Mol. Str. 1127 (2017) 6-14.

[24] S.Zh. Karazhanov, P. Ravindran, P. Vajeeston, A.G. Ulyashin, H. Fjellvag and B.G. Svensson, Phase stability and pressure-induced structural transitions at zero temperature in $ZnSiO_3$ and Zn_2SiO_4, J. Phys.: Condens. Matter 21 (2009) 485801 (9pp).

[25] R. Chandramohan, V. Dhanasekaran, R. Arumugam, K. Sundaram, J. Thirumalai, T. Mahalingam, Properties Evaluation of Annealed $ZnAl_2O_4$ Alloy Thin Films, Dig. J. Nan. Bios. 7 : 3 (2012) 1315 -1325.

[26] S.Y. Hu, Y.C. Lee, J.W. Lee, J.C. Huang, J.L. Shen, W. Water, The structural and optical properties of ZnO/Si thin films by RTA treatments, App. Sur. Sci. 254 (2008) 1578–1582.

[27] Z.B. Fang, Z.J. Yan, Y.S. Tan, X.Q. Liu, Y.Y. Wang, Influence of post- annealing treatment on the structure properties of ZnO films, App. Sur. Sci. 241 (2005) 303–308.

[28] Ş. Talu, M. Bramowicz, S. Kulesza, S. Solaymani, A. Ghaderi, L. Dejam, S.M. Elahi, A. Boochani, Microstructure and micromorphology of ZnO thin films: Case study on Al doping and annealing effects, Super. Micros. 93 (2016) 109-121.

[29] M. eh, H-C. Chen, M-J Chen, J-R. Yang and M. Shiojiri, Structure and Electro-Optical Properties of Thin Films Grown by Alternate Atomic Layer Deposition of ZnO and Al_2O_3 on the Sapphire Substrate, Mater. Trans.: Special Issue on Development and Fabrication of Advanced Materials Assisted by Nanotechnology and Microanalysis, 51: 2 (2010) 219-226.

[30] M.F. Malek, M.H. Mamat, M.Z. Musa, Z. Khusaimi, M.Z. Sahdan, A.B. Suriani, A. Ishak, I. Saurdi, S.A. Rahman, M. Rusop, Thermal annealing-induced formation of ZnO nanoparticles:Minimum strain and stress ameliorate preferred c-axis orientation and crystal-growth properties, J. All. Comp. 610 (2014) 575–588.

[31] S. Iaiche and A. Djelloul, ZnO/$ZnAl_2O_4$ Nanocomposite Films Studied by X-Ray Diffraction, FTIR, and X-Ray Photoelectron Spectroscopy, J. Spectr. (2015).

[32] D.I. Rusu, G.G. Rusu and D. Luca, Structural Characteristics and Optical Properties of Thermally Oxidized Zinc Films, Act. Phys. Polo. A, 119: 6 (2011).

[33] P. Kumar, A. Singh, D. Pathak, L. Hromadko, T. Wagner, Structural and optical properties of sol-gel processed ZnCdMgO nanostructured films as transparent conductor, Adv. Mater. Lett. 5(10) (2014).

[34] P.C. Dorsey, B.J. Rappoli, K.S. Grabowski, P. Lubitz, D.B. Chrisey, and J.S. Horwitz, J. Appl. Phys. 81 (1997) 6884.

[35] A. Bouhemadou, R. Khenata, Phys. Lett. A, 360 (2006) 339–343.

[36] A.B. Usseinov, E.A. Kotomin, A.T. Zhukovskii and J. Puans, T. Sol. Fil. 553 (2014) 38–42.

[37] G. Kaur, A. Mitra and K.L. Yadav, Pulsed laser deposited Al-doped ZnO thin films for optical applications, Prog. in Nat. Sci.: Mater. Inter. 25 (2015) 12–21.

[38] K. Nadeemn, S.Rahman and M. Mumtaz, Effect of annealing on properties of Mg doped Zn-ferrite nanoparticles, Prog. in Nat. Sci.: Mater. Inter. 25 (2015) 111–116.

[39] M. Bizarro and S.E. Rodi, New Visible-Light Active Semiconductors, Photocatalytic Semiconductors: Synthesis, Characterization, and Environmental Applications, Springer, 2015, pp. 103-155. Chapter 4 Physicochemical Characterization of Photocatalytic Materials, in: A. Hernández-Ramírez, I. Medina-Ramírez (Eds.).

[40] V. Savunthari Kirankumar, S. Sumathi, Catalytic activity of bismuth doped zinc aluminate nanoparticles towards environmental remediation, Mater. Res. Bull. 93 (2017) 74–82.

[41] M. Ebrahimizadeh Abrishami, S.M. Hosseini, E. Attarankakhki and M. Ghasemifards, Synthesis and structure of pure and Mn-doped zinc oxide nanopowders, Inter. J. Nan. 9: 1 & 2 (2010) 19–28.

[42] A. Djelloul, M-S. Aida, J. Bougdira, Photoluminescence, FTIR and X-ray diffraction studies on undoped and Al-doped ZnO thin films grown on polycrystalline α-alumina substrates by ultrasonic spray pyrolysis, J. Lum. 130 (2010) 2113–2117.

[43] K. Bouzid, A. Djelloul, N. Bouzid, J. Bougdira, Electrical resistivity and photoluminescence of zinc oxide films prepared by ultrasonic spray pyrolysis, Phys.Stat. Sol. A, 206: 1 (2009) 106–115.

[44] D. Djouadi, A. Chelouche, A. Aksas, Amplification of the UV Emission of ZnO: Al Thin Films Prepared by Sol-Gel Method, J. Mater. Environ. Sci. 3: 3 (2012) 585-590.

[45] C.M. Fang, C-K. Loong, G.A. de Wijs, and G. de With, Phonon spectrum of $ZnAl_2O_4$ spinel from inelastic neutron scattering and first-principles calculations, Phys. Rev. B 66, 144301 (2002).

[46] K. Hoggas, C. Nouveau, A. Djelloul, M. Bououdina, Structural, microstructural, and optical properties of $Zn_{1-x}Mg_xO$ thin films grown onto glass substrate by ultrasonic spray pyrolysis, Appl. Phys. A, 120 (2015) 745–755.

[47] H. Yu, J. Yu, B. Cheng, M. Zhou, Effects of hydrothermal post-treatment on microstructures and morphology of titanate nanoribbons, Journal of Solid State Chemistry, 179 (2006) 349–354.

[48] A. Abdalla, S. Bereznev, N. Spalatu, O. Volobujeva, N. Sleptsuk & M. Danilson, Pulsed laser deposition of Zn(O,Se) layers in nitrogen background Pressure, 9:17443 (2019).

[49] H.W. Lee, S.P. Lau, Y.G. Wang, B.K. Tay, H. H. Hang, T. Sol. Fil. 458 (2004).

[50] W.Y. Liang, A.D. Yoffe, Phys. Rev. Lett. 20 (1968) 59.

[51] M. Kumar, V. Natarajan and S.V Godbole, Synthesis, characterization, photoluminescence and thermally stimulated luminescence investigations of orange red-emitting Sm^{3+} doped $ZnAl_2O_4$ phosphor, Bull. Mater. Sci. 37: 6 (2014) 1205–1214.

[52] A.A. Letailleur, S. Yu Grachev, E. Barthel, E. Sondergard, K. Nomenvo, High Efficiency White Luminescence of Alumina doped ZnO, J. Lum. 131: 12 (2011) 2646-2651.

[53] J.P. Roucan et M-C. N-Dutrioux, Proppriétés physico-chimiques (K1) Article : Propriétés physiques des composés minéraux, 82 (2010).

[54] Handbook of Chemistry and Physics, 56th Edition, Ed. R.C. Weast, CRS Press, 1975.

[55] B. Chandra Babu, S. Buddhudu, Emission spectra of Tb^{3+}: Zn_2SiO_4 and Eu^{3+}: Zn_2SiO_4 sol-gel powder phosphors, J. Spectr. Dyn. 4: 5 (2014).

[56] C. Xu, J. Chun, K. Rho and D. Eon Kim, Fabrication and photoluminescence of zinc silicate/silica modulated ZnO nanowires, Nanot. 16 (2005) 2808–2812.

[57] A-M. Ali, A.A. Ismail, R. Najmy, A. Al-Hajry, Preparation and characterization of ZnO–SiO_2 thin films as highly efficient photocatalyst, J. Photochem. Photob. A: Chem. 275 (2014) 37–46.

[58] V. D'Ippolito, G. B. Andreozzi, F. Bosi, U. Hålenius, L. Mantovani, D. Bersani and R.A. Fregola, Crystallographic and spectroscopic characterization of a natural Zn-rich spinel approaching the endmember gahnite ($ZnAl_2O_4$) composition, Mineral. Mag. 77(7) (2013) 2941–2953.

[59] V. D'Ippolito, G.B. Andreozzi, D. Bersani and P.P. Lottici, Raman fingerprint of chromate, aluminate and ferrite spinels, J. Ram. Spectr. (2015).

[60] D. Errandonea, Chapter 2 AB_2O_4 Compounds at High Pressures, Pressure-Induced Phase Transitions in AB_2X_4 Chalcogenide Compounds, F. J. Manjon, I. Tiginyanu, V. Ursaki (Eds), XIII.

[61] T.B. Ivetić, M.R. Dimitrievska, I.O. Gúth, Lj.R. -Dačanin, S.R. Lukić-Petrović, Structural and optical properties of europium-doped zinc oxide nanopowders prepared by mechanochemical and combustion reaction methods, J. Res. in Phys. 36: 1 (2012) 43-51.

[62] O. Lupan, L. Chow, L.K. Ono, B.R. Cuenya, G. Chai, H. Khallaf, S. Park, A. Schulte, Synthesis and Characterization of Ag- or Sb-Doped ZnO Nanorods by a Facile Hydrothermal Route, J. Phys. Chem. C, 114 (2010) 12401–12408.

[63] D.N. Montenegro, V. Hortelano, O. Martínez, M.C. Martínez-Tomas, V. Sallet, V. Muñoz-Sanjosé, J. Jiménez, Non-radiative recombination centres in catalyst-free ZnO nanorods grown by atmospheric-metal organic chemical vapour deposition, J. Phys. D: Appl. Phys. 46 (2013) 235302.

[64] K.J. Chen, T.H. Fang, F.Y. Hung, L.W. Ji, S.J. Chang, S.J. Young, Y.J. Hsiao, The crystallization and physical properties of Al-doped ZnO nanoparticles, App. Sur. Sci. 254 (2008) 5791–5795.

[65] S. Kunj, K. Sreenivas, Residual stress and defect content in magnetron sputtered ZnO films grown on unheated glass substrates, Cur. App. Phys. 16: 7 (2016). DOI: 10.1016/j.cap.2016.04.008.

[66] I. Musa, N. Qamhieh, S. Thaker Mahmoud, Synthesis and length dependent photoluminescence property of zinc oxide nanorods, Res. in Phys. 7 (2017) 3552–3556.

[67] F-C. Liu, J-Y. Li, T-H. Chen, C-H. Chang, C-T. Lee, W-H. Hsiao and D-S. Liu, Effect of Silver Dopants on the ZnO Thin Films Prepared by a Radio Frequency Magnetron Co-Sputtering System, Mater. 10: 797 (2017).

[68] A. Khan, Raman Spectroscopic Study of the ZnO Nanostructures, J. Pak. Mater. Soc., 4: 1 (2010).

[69] A. Mossad Ali, A.A. Ismail, R. Najmye, A. Al-Hajry, Preparation and characterization of ZnO–SiO_2 thin films as highly efficient photocatalyst, Journal of Photochemistry and Photobiology A: Chem. 275 (2014) 37–46.

[70] V. Postica, A. Vahl, D. Santos-Carballal, T. Dankwort, L. Kienle, M. Hoppe, A. Cadi-Essadek, N.H. de Leeuw, M-I. Terasa, R. Adelung, F. Faupel, O. Lupan, Tuning ZnO Sensors Reactivity toward Volatile Organic Compounds via Ag Doping and Nanoparticle Functionalization, ACS Appl. Mater. Inter. 12(12):12 (2019).

[71] B. Chandra Babu, S. Buddhudu, Analysis of structural and electrical properties of Ni^{2+}:Zn_2SiO_4 ceramic powders by sol–gel method, J. Sol-Gel Sci. Technol. (2014).

[72] M. Zhang, Raman Spectroscopy and Applications, Chapter 5: Raman Study of the Crystalline-to Amorphous State in Alpha-Decay-Damaged Materials, INTECH, (2017).

[73] S. Lopez-Moreno, P. Rodriguez-Hernandez, A. Muñoz, A.H. Romero, F.J. Manjon, D. Errandonea, E. Rusu, V.V. Ursaki, Lattice dynamics of $ZnAl_2O_4$ and $ZnGa_2O_4$ under high pressure, Ann. Phys. 523: 1-2 (2011) 157–167.

[74] A. Chopelas, A.M. Hofmeister, Vibrational spectroscopy of aluminate spinels at 1 atm and of $MgAl_2O_4$ to over 200 kbar. Phys. Chem. Min. 18 (1991) 279-293.

[75] A. Giussani, P. Zaumseil, O. Seifarth, P. Storck, T. Schroeder, A novel engineered oxide buffer approach for fully lattice-matched SOI heterostructures, New J. Phys.12 (2010) 093005.

[76] K. Chitrarasu, J. Udaya Bhanu, R. Dhanabal, A. Chandrabose, P. Thangadurai, Structural evolution and electrical properties of the biphasic compound α-Al_2O_3:$MgAl_2O_4$, Mater. Res. Bull. 90 (2017) 244–252.

[77] K.R. Nagabhushana, B.N. Lakshminarasappa, F. Singh, Photoluminescence and Raman studies in swift heavy ion irradiated polycrystalline aluminum oxide, Bull. Mater. Sci. 32: 5 (2009) 515–519.